ACS APPLIED MATERIALS & INTERFACES

Research Article

www.acsami.org

Manipulating Crystallization of Organolead Mixed-Halide Thin Films in Antisolvent Baths for Wide-Bandgap Perovskite Solar Cells

Yuanyuan Zhou,[†,‡] Mengjin Yang,[‡,§] Onkar S. Game,[†] Wenwen Wu,[†] Joonsuh Kwun,[†] Martin A. Strauss,[†] Yanfa Yan,[∥] Jinsong Huang,[⊥] Kai Zhu,[*,§] and Nitin P. Padture[*,†]

[†]School of Engineering, Brown University, Providence, Rhode Island 02912, United States

[§]Chemistry and Nanoscience Center, National Renewable Energy Laboratory, Golden, Colorado 80401, United States

[∥]Department of Physics and Astronomy and Wright Center for Photovoltaics Innovation and Commercialization, University of Toledo, Toledo, Ohio 43606, United States

[⊥]Department of Mechanical and Materials Engineering, Nebraska Center for Materials and Nanoscience, University of Nebraska−Lincoln, Lincoln, Nebraska 68588, United States

Supporting Information

ABSTRACT: Wide-bandgap perovskite solar cells (PSCs) based on organolead (I, Br)-mixed halide perovskites (e.g., $MAPbI_2Br$ and $MAPbIBr_2$ perovskite with bandgaps of 1.77 and 2.05 eV, respectively) are considered as promising low-cost alternatives for application in tandem or multijunction photovoltaics (PVs). Here, we demonstrate that manipulating the crystallization behavior of (I, Br)-mixed halide perovskites in antisolvent bath is critical for the formation of smooth, dense thin films of these perovskites. Since the growth of perovskite grains from a precursor solution tends to be more rapid with increasing Br content, further enhancement in the nucleation rate becomes necessary for the effective decoupling of the nucleation and the crystal-growth stages in Br-rich perovskites. This is enabled by introducing simple stirring during antisolvent-bathing, which induces enhanced advection transport of the extracted precursor-solvent into the bath environment. Consequently, wide-bandgap planar PSCs fabricated using these high quality mixed-halide perovskite thin films, Br-rich $MAPbIBr_2$, in particular, show enhanced PV performance.

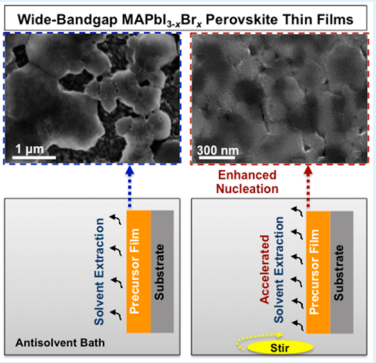

KEYWORDS: *antisolvent−solvent extraction, nucleation, grain growth, solar cells, wide-bandgap perovskite*

1. INTRODUCTION

Perovskite solar cells (PSCs) have attracted a great deal of interest due to their low-temperature solution-processability and high power conversion efficiencies (PCEs).[1−8] While the lower-bandgap (~1.5 eV) organolead triiodide perovskite, $CH_3NH_3PbI_3$ ($MAPbI_3$), absorber has been studied extensively for the purpose of realizing the highest PCEs in single-junction solar cells,[1−8] (I, Br)-mixed halide perovskites with wider bandgaps show promise for application in tandem or multijunction solar cells.[9−13] Among these mixed halide perovskites, $CH_3NH_3PbI_2Br$ ($MAPbI_2Br$) and $CH_3NH_3PbIBr_2$ ($MAPbIBr_2$) perovskites, with bandgaps of 1.77 and 2.05 eV, respectively,[14] are particularly interesting compositions that are near-ideal for application as the top-cell absorber materials in tandem and triple-junction solar cells.[9−13,15,16]

Since the morphology of the perovskite absorber thin film is one of the most critical factors that influence the overall PCE of PSCs,[17−19] unprecedented amount of effort has been devoted toward controlling perovskite crystallization for improved film uniformity, and gaining better understanding of these processes.[1−4] In the case of the $MAPbI_3$, it has been shown that inducing rapid nucleation of perovskite crystals at room temperature through antisolvent treatments, which enables better decoupling of the nucleation and the growth stages, is an effective way to achieve large-area, pinhole-free $MAPbI_3$ films, and it is proving to be a promising processing protocol.[20−26] In a recent report, we studied the room-temperature crystallization behavior of $MAPbI_3$ perovskite in antisolvent baths,[22] and showed that uniform precipitation of $MAPbI_3$ in the antisolvent environment, coupled with the 'antisolvent−solvent extraction' process, results in the formation of ultrasmooth, dense perovskite thin films.[22] The enhanced nucleation of the solid perovskite over the entire substrate area upon contact of the precursor film with the antisolvent in the bath is crucial for achieving large-area uniformity in these $MAPbI_3$ perovskite thin films.[25,26] This is, to some extent, similar to what occurs in the "solvent-dripping" process reported by Jeon et al.[23] and Xiao et al.[21] While the solution crystallization behavior has been studied extensively, it is almost exclusively limited to $MAPbI_3$ perovskite thin films, with only a handful of reports dealing with (I, Br)-mixed halide perovskite thin films.[10,12,13] It has been observed by others[27,28] and by us (Figure S1 in

Received: November 13, 2015
Accepted: January 4, 2016
Published: January 4, 2016

DOI: 10.1021/acsami.5b10987
ACS Appl. Mater. Interfaces 2016, 8, 2232−2237

Supporting Information (SI)) that with the increase in the Br content, the perovskite grains tend to grow in an exaggerated fashion from the precursor solution, which results in the formation of incomplete coverage and pinholes. While a number of factors (ions, bond energies, solvation, etc.) may be responsible for this, the most basic explanation is that the growth of perovskite crystals is mainly driven by the diffusion of the ions to the as-formed nuclei.[29] Since Br^- (r = 1.96 Å)[28] has a smaller ionic radius than I^- (r = 2.20 Å),[30] the diffusivity of Br^- (D_{Br-}) in the solvent is expected to be higher than I^- (D_{I-}) according to the Stokes–Einstein equation, $D = \frac{k_B T}{6\pi\eta r}$, where k_B is the Boltzmann's constant, T is the absolute temperature, η is the dynamic viscosity of the solution, and r is ionic radius.[31] Thus, faster overall growth kinetics of perovskite grains in the Br-rich precursor solution, as compared with the I-rich precursor solution, are expected. In order to enhance the uniformity of the (I, Br)-mixed halide perovskite thin films, it is necessary to accelerate further the nucleation rate for better decoupling of the nucleation and the grain growth stages. Since antisolvent–solvent extraction is one of the important factors that induces supersaturation and nucleation in this method,[22] the nucleation rate is expected to be enhanced by stirring the antisolvent bath. Such continuous mechanical perturbation enables rapid advection transport of extracted precursor-solvent, which maximizes the concentration gradient across the precursor-film/antisolvent interface and promotes rapid mixing of the precursor-solvent into antisolvent in the bath. Here we show that stirring is particularly important in the case of Br-rich perovskites, as compared to I-rich perovskites, in obtaining dense, pinhole-free, thin films. Planar PSCs incorporating mixed-halide perovskite thin films of Br-rich composition ($MAPbIBr_2$), in particular, synthesized using this accelerated "antisolvent–solvent extraction" method, show enhanced PV performance.

2. EXPERIMENTAL SECTION

2.1. Crystallization of Mixed-Halide Perovskite Thin Films. A solution (30 wt %) of PbI_2 (Alfa-Aesar, Ward Hill, MA) and MABr (molar ratio 1:1) in n-methyl-2-pyrrolidone (NMP) was spin-coated onto compact-TiO_2-coated FTO glass substrates (Hartford Glass Co., Hartford City, IN), which was immediately followed by immersing the film in a bath (1000 mL) of anhydrous diethyl ether (DEE; Fisher Scientific, Fair Lawn, NJ) antisolvent at room temperature. In order to introduce advection in the antisolvent bath, magnetic stirring (400 rpm) was used. Within 30 s, $MAPbI_2Br$ perovskite thin film was formed. The substrate was then taken out of the bath and dried rapidly under blowing nitrogen gas. For the preparation of $MAPbIBr_2$ thin films, a precursor solution (30 wt %) of $PbBr_2$ (Alfa-Aesar, Ward Hill, MA) and MAI (molar ratio 1:1) was used and dipped in stirred DEE antisolvent bath for 15 s.

2.2. Materials Characterization. X-ray diffraction (XRD) was performed on a X-ray diffractometer (D8-Advance, Bruker, Germany) using Cu $K\alpha_1$ radiation (λ = 1.5406 Å) at step size/time 0.02°/1 s conditions. Surface morphology of the films and cross sections (fractured) of the whole solar cells were observed in a scanning electron microscope (SEM; LEO 1530VP, Carl Zeiss, Germany). The local roughness of the perovskite thin films were characterized using an atomic force microscope (AFM; 5500, Agilent, Santa Clara, CA) operated in noncontact mode. Optical spectroscopy (transmission, refection, absorption) was conducted on a UV-vis-NIR spectrophotometer equipped with diffuse reflectance accessories (Cary 6000i, Agilent Technologies, Englewood, CO) with 10 nm step size. Transmission electron microscopy (TEM) was used to characterize cross sections of the whole PSCs. Note that this particular PSC has a thinner HTM layer compared to most of the other PSCs fabricated in this study. TEM specimens from specific locations on the cross sections were prepared by focused ion beam (FIB; Helios 600, FEI, Hillisboro, OR) and extracted by in situ lift-out. These specimens were examined using a TEM (2100F, JEOL, Japan) operated at 200 kV accelerating voltage. Fourier-transform infrared (FTIR) spectra are recorded on a spectrometer (4100, Jasco Instruments, Easton, MD). The powder sample used for FTIR was scratched from a relatively thick spin-coated films (30 wt % precursor solution, 2000 rpm, 10 s).

2.3. Device Fabrication and Characterization. For the fabrication of the PSCs, a compact-TiO_2 electron selective layer (ESL) was first deposited on prepatterned FTO-coated glass by spray pyrolysis at 450 °C. The perovskite layer was then optimally deposited based on the procedure described above, followed by spin-coating a hole-transporting material (HTM) solution, which consisted of 80 mg 2,2′,7,7′-tetrakis(*N*,*N*-dip-methoxyphenylamine)-9,9′-spirobifluorene (Spiro-MeOTAD), 30 μL bis(trifluoromethane) sulfonimide lithium salt stock solution (500 mg Li-TFSI in 1 mL acetonitrile), 30 μL of 4-*tert*-butylpyridine (TBP), and 1 mL of chlorobenzene solvent. The HTM spin-coating process was performed in a dry-air atmosphere with humidity < 10%. Finally, a ∼150 nm Ag layer was deposited using thermal evaporator and a shadow mask. The incident photon-to-current efficiency (IPCE) or external quantum efficiency (EQE) spectra were recorded at a chopping frequency of 5 Hz in AC mode on a solar cell quantum efficiency measurement system (QEX10, PV Measurements, Boulder, CO). The current density (J)–voltage (V) characteristics of the cells were obtained using a 2400 SourceMeter (Keithley, Cleveland, OH) under simulated one-sun AM 1.5G illumination (100 mW cm^{-2}) (Oriel Sol3A Class AAA Solar Simulator, Newport Corporation, Irvine, CA). Typical J–V scan started from short-circuit to forward-bias and then back to short-circuit at the rate of 20 mV s^{-1}. The maximum-power output stability of the solar cells was measured by monitoring J output at the maximum-power V bias using a VersaSTAT MC potentiostat (Princeton Applied Research, Acton, MA). A shutter was used to control the one-sun illumination on the PSC. A typical active area of 0.12 cm^2 was defined using a nonreflective mask for the J–V measurements.

3. RESULTS AND DISCUSSION

Figure 1A and B show schematic illustrations of the standard and accelerated "antisolvent–solvent extraction" processes, respectively. In the standard procedure (Figure 1A), the spin-coated NMP solution film of $MAPbI_{3-x}Br_x$ mixed halide perovskite is dipped vertically in a large bath of DEE

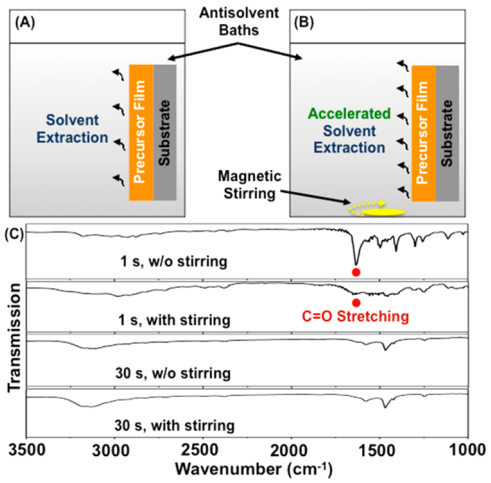

Figure 1. Schematic illustration of the crystallization of perovskite in antisolvent bath: (A) standard process without stirring; (B) accelerated process with magnetic stirring; (C) FTIR spectra of the as-formed film after 1 and 30 s dipping in antisolvent baths with and without stirring.

DOI: 10.1021/acsami.5b10987
ACS Appl. Mater. Interfaces 2016, 8, 2232–2237

antisolvent. This is identical to what we have reported in the case of $MAPbI_3$.[22] The supersaturation of $MAPbI_{3-x}Br_x$ in the NMP solution is induced immediately upon contact with the DEE antisolvent, which is highly miscible with the precursor solvent NMP. The relatively small amount of NMP solvent diffuses into the large-volume DEE bath; this is referred to as the "antisolvent−solvent extraction" process. This ambient process contributes to the enhancement of the rate of nucleation of solid perovskite, compared with the conventional solution crystallization processes at higher temperatures that promote crystal growth over nucleation.[22] In Figure 1B, continuous mechanical perturbation is introduced in the DEE antisolvent bath by using simple magnetic-stirring. With stirring, the DEE solvent continuously swipes across precursor-film surface for advection transport of the extracted NMP, which is more rapid than the unforced diffusion process. This advection transport of NMP is also expected to induce abrupt mass gradient across the NMP−DEE interface, which facilitates the extraction of NMP out of the precursor films. The accelerated extraction of NMP is confirmed by FTIR measurements ($MAPbI_2Br$ is demonstrated here as an example). Figure 1C shows an FTIR spectrum from the $MAPbI_2Br$ perovskite precursor film after 1 s dipping without stirring. A strong band, corresponding to C═O stretching, is observed in that FTIR spectrum, which indicates that a relatively large amount of NMP is still present in the film.[22] However, when dipped in the stirring bath for 1 s, the intensity of this band is significantly reduced, and better-resolved characteristics of the perovskite appear in the spectrum. This indicates that the perturbation of antisolvent by stirring has accelerated the rate of precursor-solvent extraction in promoting the nucleation of solid perovskite. FTIR spectra for the film dipped for 30 s in the antisolvent bath with and without stirring are shown in Figure 1C. Both exhibit typical perovskite features with no obvious presence of NMP, indicating that the antisolvent−solvent extraction is complete in 30 s. Note that this time period is much shorter compared with the $MAPbI_3$ case (2 min),[22] which is consistent with the accelerated growth kinetics with increasing Br content.

Figure 2 shows XRD patterns of the as-crystallized perovskites thin films. Phase-pure $MAPbI_2Br$ or $MAPbIBr_2$ perovskite is observed in all the films, indicating that crystallization of the perovskites is complete under these experimental conditions. The bandgap of crystallized $MAPbI_2Br$ and $MAPbIBr_2$ is confirmed to be 1.77 and 2.05 eV, respectively, from the Tauc plots shown in Figure S2 in SI.

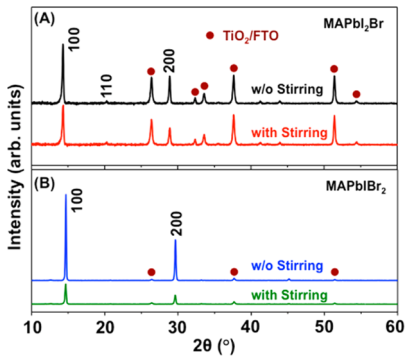

Figure 2. XRD patterns of as-crystallized (A) $MAPbI_2Br$ and (B) $MAPbIBr_2$ thin films with and without stirring of the antisolvent bath.

Note that 15 s dipping time appears to be adequate in the case of $MAPbIBr_2$ films under the same condition, while 30 s dipping time is necessary for the $MAPbI_2Br$ films. The characteristic (200) peak in the XRD patterns from the $MAPbIBr_2$ film appears sharper (fwhm: 0.17° without stirring, 0.20° with stirring) than that from $MAPbI_2Br$ films (fwhm: 0.23° without stirring, 0.26° with stirring), as shown in Figure S3 in SI, indicating better crystallinity in the $MAPbIBr_2$ films overall. The characteristic XRD peaks in both films are indexed according to cubic perovskite symmetry ($Pm\bar{3}m$). The characteristic $MAPbI_2Br$ (100) peak in Figure 2A has shifted to higher 2θ in $MAPbIBr_2$ in Figure 2B, corresponding to a reduction in the lattice parameter from a = 0.616 nm to a = 0.604 nm with the increase in the Br content, which is consistent with what is reported in the literature.[11] The effect of stirring on the crystallinity of the as-formed mixed-halide perovskites is also revealed in the XRD patterns. In the case of the $MAPbI_2Br$ films (Figure 2A), the diffraction peaks without stirring appears to be slightly sharper and more intense compared to those with stirring. With its higher Br content (in the $MAPbIBr_2$ case), the difference is much more evident (Figure 2B). The broader XRD peak (0.20° fwhm for (200) peak) in the stirred $MAPbIBr_2$ case compared with the nonstirred case (0.17° fwhm) suggests finer microstructure, although the grain size appears to be beyond the validity of quantitative analysis using the Scherer equation.[32]

The surface morphology of the perovskite film is examined using scanning electron microscopy (SEM) and atomic force microscopy (AFM), and the results are presented in Figure 3. In Figure 3A,C, the film produced without stirring is composed of ∼100 nm grains with occasional large grains (∼250 nm), while for the stirred case, the grains are more uniform in size (∼100 nm). The overall roughness of both $MAPbI_2Br$ films produced without (Figure 3A,B) and with (Figure 3C,D) stirring is similar (∼9 nm). Note that, similar to the $MAPbI_3$ case,[22] the overall coverage and uniformity of the mixed-halide films from the antisolvent-bathing route are much better than those obtained from simple thermally driven solution crystallization (Figure S4 in SI). In the case of $MAPbIBr_2$, the as-crystallized film without stirring exhibits poor coverage, with large gaps between micron-sized large grains (Figure 3E). However, when stirring is introduced in the formation process of the $MAPbIBr_2$ thin films, the coverage is improved significantly, resulting in a more compact film (Figure 3G). Also, the roughness of the $MAPbIBr_2$ thin films decreases from ∼160 nm (Figure 3F) to ∼15 nm (Figure 3H). The apparent grain size of $MAPbIBr_2$ film in the stirred case is much smaller (∼300 nm). These AFM and SEM results suggest fine grain structures exist in those perovskite thin films produced from stirred baths, which is consistent with the relatively less intense XRD peaks in those films as discussed above.

The above results (FTIR, XRD, SEM, AFM) suggest the obvious effect of acceleration in the antisolvent−solvent extraction on the final thin film morphology of $MAPbI_{3-x}Br_x$ perovskites, which becomes even more pronounced for the Br-richer perovskites. To clarify this effect, the proposed processes for nucleation and grain growth of Br-rich perovskite thin films in antisolvent baths are shown schematically in Figure 4. In a stationary antisolvent bath (Figure 4A), the number of the nuclei on the substrate is few, which rapidly grow into large $MAPbI_{3-x}Br_x$ grains due to the fast diffusion of ions toward the nuclei. Assuming Volmer−Weber growth, those grains eventually result in the formation of "islands" with gaps in

DOI: 10.1021/acsami.5b10987
ACS Appl. Mater. Interfaces 2016, 8, 2232−2237

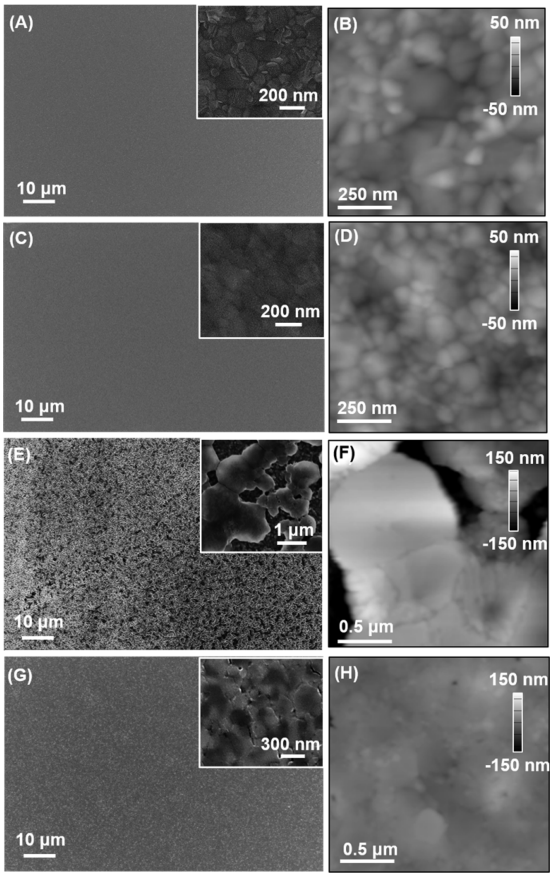

Figure 3. SEM images of the top surface of as-crystallized $MAPbI_2Br$ thin films: (A) without and (C) with stirring of the antisolvent bath; SEM images of the top surface of as-crystallized $MAPbIBr_2$ thin films: (E) without and (G) with stirring. AFM images in (B), (D), (F), and (H) correspond to SEM images in (A), (C), (E), and (G), respectively.

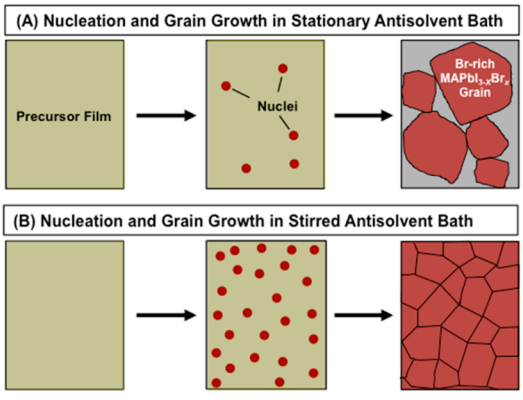

Figure 4. Proposed processes for nucleation and grain growth of Br-rich perovskite thin films in antisolvent baths: (A) stationary and (B) stirred.

between (see Figure 3E). However, when stirring is introduced in the bath, the nucleation rate is expected to increase due to accelerated antisolvent–solvent extraction (see Figure 1C), in which case a higher concentration of nuclei are expected to be uniformly distributed all over the substrate. Consequently, these nuclei grow into grains and ultimately coalesce into a dense polycrystalline grain structure in the thin film (see Figure 3G). Note that in this discussion it has been assumed that classical nucleation and growth are at play, considering the paucity of data on nucleation and growth in the solution processing of hybrid perovskites proving otherwise.[25] There are several nonclassical mechanisms[33] that could also be involved, but the identification of those mechanisms in the context of hybrid perovskites await detailed in situ characterization studies and quantitative nucleation/growth experiments.[25]

In order to assess the quality of the above mixed-halide perovskite thin films, planar PSCs were fabricated and tested. Here, perovskite thin film is sandwiched between compact-TiO_2 ESL and spiro-OMeTAD HTM layer to form a typical planar PSC, with FTO-coated glass and Ag electrodes on either side. The morphology of a PSC based on $MAPbI_2Br$ thin film produced from a stirred antisolvent bath is studied here as an example. Figure 5A is a cross-sectional TEM image of the PSC

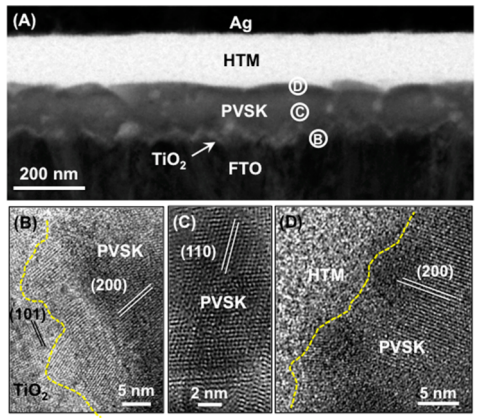

Figure 5. (A) Cross-sectional TEM image of a typical planar PSC based on $MAPbI_2Br$ perovskite thin film (stirred antisolvent bath). The FTO, TiO_2-ESL, perovskite (PVSK), HTM, and Ag layers are marked. (B–D) HRTEM images of the regions marked in (A).

showing the FTO, ESL, perovskite, HTMs, and Ag layers. The compactness of the perovskite absorber layer is apparent from this micrograph. The perovskite–HTM interface, the perovskite layer, and the perovskite–TiO_2 interface are examined using high-resolution TEM (HRTEM), and the images from that study are shown in Figure 5B, C, and D, respectively. In Figure 5C, (200) and (110) planes are indexed based on the interplanar spacings of 0.31 and 0.44 nm for the perovskite, respectively. The indexed (101) planes within the TiO_2 ESL (Figure 5B) and the amorphous nature of the organic HTM layer (Figure 5D) are visible. The compact perovskite layer extends from the ESL to the HTM layer, with abrupt interfaces between the layers indicating intimate contact. These represent high-quality charge-transport paths and junctions in the PSC, which are the important characteristics of an efficient photovoltaic device.

Figure 6 shows the $J-V$ characteristics of the PSCs based on $MAPbI_2Br$ and $MAPbIBr_2$ thin films without and with stirring and their corresponding EQE spectra. Overall, PSCs based on mixed-halide perovskite films produced from stirred baths show improved PCEs (see Table S1 in SI for the statistics of the PV performance parameters). Since there is no striking difference between the $MAPbI_2Br$ films produced without or with stirring, there is only a small increase in the typical PSC PCE (from 9.3% to 10.5%), which may be associated with the more uniform and dense microstructure formed under accelerated solvent extraction. In contrast, the effect of stirring is dramatic

DOI: 10.1021/acsami.5b10987
ACS Appl. Mater. Interfaces 2016, 8, 2232–2237

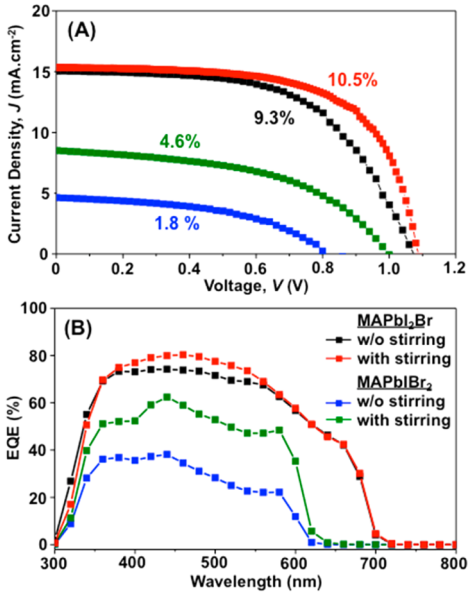

Figure 6. (A) J–V characteristics of PSCs based on $MAPbI_2Br$ and $MAPbIBr_2$ thin films at reverse scan made without and with antisolvent bath stirring and (B) the corresponding EQE spectra.

in $MAPbIBr_2$-based PSCs, as evinced by over 2-fold increase in the PCE, from 1.8 to 4.6%. This is attributed to the reduced porosity and pinholes, and better coverage in the films as discussed earlier, although other factors (e.g., grain size, thickness variation) may have some effects. Typical hysteresis is observed in these planar cells as shown in Figure 7A, and thus, the maximum-power-point power output is monitored under continuous illumination. The typical $MAPbI_2Br$-based

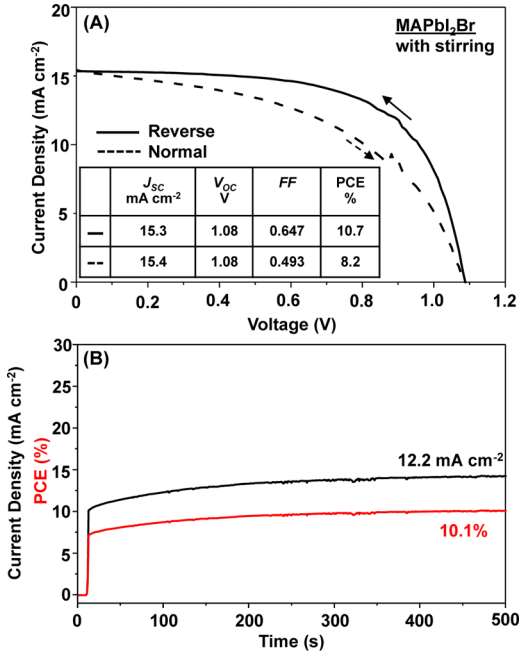

Figure 7. (A) J–V hysteresis of the typical PSC made using $MAPbI_2Br$ perovskite thin films from a stirred antisolvent bath. The inset table shows the extracted PV parameters from both normal and reverse scans; (B) The stabilized maximum-power-point current/power outputs of the typical PSC made using $MAPbI_2Br$ perovskite thin films from a stirred antisolvent bath.

PSC produced from a stirred antisolvent bath shows a stabilized PCE of 10.1% (Figure 7B). It is interesting that the wider-bandgap PSCs do not necessarily show higher open-circuit voltage (V_{OC}), which could be due to the following: (i) the Br-richer $MAPbI_{3-x}Br_x$ perovskite film appears to be less perfect in morphology as discussed above, and (ii) fine-grain (I, Br)-mixed halide perovskites under illumination may exist as segregated phases, within which those lower-bandgap, I-rich domains pin the V_{OC}.[34−36] Thus, optimization of the processing conditions (e.g., solvent selection, bath volume, stirring speed, etc.) and solutions for retarding perovskite phase segregation (e.g., grain coarsening,[34] etc.) for each specific composition may result into higher-performance wide-bandgap PSCs, which are subjects for future research.

CONCLUSIONS

We have demonstrated a facile antisolvent-bathing approach for the fabrication of high quality organolead (I, Br)-mixed halide perovskite thin films. $MAPbI_2Br$ and $MAPbIBr_2$ perovskites with bandgaps of 1.77 and 2.05 eV, respectively, are studied as example compositions. Since the antisolvent−solvent extraction plays an important role in the room-temperature nucleation of solid perovskite during antisolvent bathing, the nucleation rate is further enhanced through advection transport of the extracted precursor-solvent in the antisolvent by simple magnetic-stirring. This is particularly important in the case of Br-rich compositions for the formation of full-coverage, dense perovskite thin films. This approach is highly versatile and it can be applied to a broad range of wide-bandgap perovskite thin films with tailored compositions, and its rapid, low-temperature nature holds promise for the future development of high-performance tandem or multijunction PVs based on PSCs.

ASSOCIATED CONTENT

Supporting Information

The Supporting Information is available free of charge on the ACS Publications website at DOI: 10.1021/acsami.5b10987.

Additional results from SEM, XRD and optical spectroscopy characterization studies, and PV-performance statistics of PSCs (PDF).

AUTHOR INFORMATION

Corresponding Authors

*E-mail: kai.zhu@nrel.gov.

*E-mail: nitin_padture@brown.edu.

Author Contributions

‡Y.Z. and M.Y. contributed equally.

Notes

The authors declare no competing financial interest.

ACKNOWLEDGMENTS

The research at Brown University and University of Nebraska was supported by the National Science Foundation (Award Nos. DMR-1305913 and OIA-1538893), and the research at the National Renewable Energy Laboratory was supported by the U.S. Department of Energy under Contract No. DE-AC36-08-GO28308. M.Y. and K.Z. acknowledge the support by the U.S. Department of Energy (DOE) SunShot Initiative under the Next Generation Photovoltaics 3 program (DE-FOA-0000990).

DOI: 10.1021/acsami.5b10987
ACS Appl. Mater. Interfaces 2016, 8, 2232−2237

REFERENCES

(1) Stranks, S. D.; Snaith, H. J. Metal-Halide Perovskites for Photovoltaic and Light-Emitting Devices. *Nat. Nanotechnol.* **2015**, *10*, 391−402.

(2) Grätzel, M. The Light and Shade of Perovskite Solar Cells. *Nat. Mater.* **2014**, *13*, 838−842.

(3) Yang, W. S.; Noh, J. H.; Jeon, N. J.; Kim, Y. C.; Ryu, S.; Seo, J.; Seok, S. I. High-Performance Photovoltaic Perovskite Layers Fabricated through Intramolecular Exchange. *Science* **2015**, *348*, 1234−1237.

(4) Kim, H.-S.; Lee, C.-R.; Im, J.-H.; Lee, K.-B.; Moehl, T.; Marchioro, A.; Moon, S.-J.; Humphry-Baker, R.; Yum, J.-H.; Moser, J. E.; Grätzel, M.; Park, N.-G. Lead Iodide Perovskite Sensitized All-Solid-State Submicron Thin Film Mesoscopic Solar Cell with Efficiency Exceeding 9%. *Sci. Rep.* **2012**, *2*, 591.

(5) Zhou, H.; Chen, Q.; Li, G.; Luo, S.; Song, T.-B.; Duan, H.-S.; Hong, Z.; You, J.; Liu, Y.; Yang, Y. Interface Engineering of Highly Efficient Perovskite Solar Cells. *Science* **2014**, *345*, 542−546.

(6) Liu, M.; Johnston, M. B.; Snaith, H. J. Efficient Planar Heterojunction Perovskite Solar Cells by Vapor Deposition. *Nature* **2013**, *501*, 395−398.

(7) Burschka, J.; Pellet, N.; Moon, S.-J.; Humphrey-Baker, R.; Gao, P.; Nazeeruddin, M. K.; Gratzel, M. Sequential Deposition as a Route to High-Performance Perovskite-Sensitized Solar Cells. *Nature* **2013**, *499*, 316−319.

(8) Kojima, A.; Teshima, K.; Shirai, Y.; Miyasaka, T. Organometal Halid Perovskites as Visible-Light Sensitizers for Photovoltaic Cells. *J. Am. Chem. Soc.* **2009**, *131*, 6050−6051.

(9) Bailie, D.; Christoforo, M. G.; Mailoa, J. P.; Bowring, A. R.; Unger, E. L.; Nguyen, W. H.; Burschka, J.; Pellet, N.; Lee, J. Z.; Grätzel, M.; Noufi, R.; Buonassisi, T.; Salleo, A.; McGehee, M. D. *Energy Environ. Sci.* **2015**, *8*, 956−963.

(10) Zhao, Y.; Zhu, K. Solution-Chemistry Engineering toward High-Efficiency Perovskite Solar Cells. *J. Phys. Chem. Lett.* **2014**, *5*, 4175−4186.

(11) Noh, J. H.; Im, S. H.; Heo, J. H.; Mandal, T. N.; Seok, S. I. Chemical Management for Colorful, Efficient, and Stable Inorganic−Organic Hybrid Nanostructured Solar Cells. *Nano Lett.* **2013**, *13*, 1764−1769.

(12) Bi, C.; Yuan, Y.; Fang, Y.; Huang, J. Low-Temperature Fabrication of Efficient Wide-Bandgap Organolead Trihalide Perovskite Solar Cells. *Adv. Energy Mater.* **2015**, *5*, 1401616.

(13) Liang, P.-W.; Chueh, C.-C.; Xin, X.-F.; Zuo, F.; Williams, S. T.; Liao, C.-Y.; Jen, A. K.-Y. High-Performance Planar-Heterojunction Solar Cells Based on Ternary Halide Large-Band-Gap Perovskites. *Adv. Energy Mater.* **2015**, *5*, 1400960.

(14) Mosconi, E.; Amat, A.; Nazeeruddin, M. K.; Grätzel, M.; De Angelis, F. First-Principles Modeling of Mixed Halide Organometal Perovskites for Photovoltaic Applications. *J. Phys. Chem. C* **2013**, *117*, 13902−13913.

(15) Green, M. A. *Third Generation Photovoltaics: Advanced Solar Conversion*; Springer: Berlin, Germany, 2006.

(16) Vivien, L.; Pavesi, L. *Handbook of Silicon Photonics*; CRC Press: Boca Raton, FL, 2013.

(17) Zhou, Y.; Yang, M.; Vasiliev, A. L.; Garces, H. F.; Zhao, Y.; Wang, D.; Pang, S.; Zhu, K.; Padture, N. P. Growth Control of Compact $CH_3NH_3PbI_3$ Thin Films via Enhanced Solid-State Precursor Reaction for Efficient Planar Perovskite Solar Cells. *J. Mater. Chem. A* **2015**, *3*, 9249−9256.

(18) Eperon, G. E.; Burlakov, V. M.; Docampo, P.; Goriely, A.; Snaith, H. J. Morphological Control for High Performance, Solution-Processed Planar Heterojunction Perovskite Solar Cells. *Adv. Funct. Mater.* **2014**, *24*, 151−157.

(19) Wang, D.; Liu, Z.; Zhou, Z.; Zhu, H.; Zhou, Y.; Huang, C.; Wang, Z.; Xu, H.; Jin, Y.; Fan, B.; Pang, S.; Cui, G. Reproducible One-Step Fabrication of Compact $MAPbI_{3-x}Cl_x$ Thin Films Derived from Mixed-Lead-Halide Precursors. *Chem. Mater.* **2014**, *26*, 7145−7150.

(20) Huang, F.; Dkhissi, Y.; Huang, W.; Xiao, M.; Benesperi, I.; Rubanov, S.; Zhu, Y.; Lin, X.; Jiang, L.; Zhou, Y.; Gray-Weale, A.; Etheridge, J.; McNeill, C.; Garuso, R. A.; Bach, U.; Spiccia, L.; Cheng, Y.-B. Gas-Assisted Preparation of Lead Iodide Perovskite Films Consisting of a Monolayer of Single Crystalline Grains for High Efficiency Planar Solar Cells. *Nano Energy* **2014**, *10*, 10−18.

(21) Xiao, Z.; Bi, C.; Shao, Y.; Dong, Q.; Yuan, Y.; Wang, C.; Gao, Y.; Huang, J. Efficient, High Yield Perovskite Photovoltaic Devices Grown by Interdiffusion of Solution-Processed Precursor Stacking Layers. *Energy Environ. Sci.* **2014**, *7*, 2619−2623.

(22) Zhou, Y.; Yang, M.; Wu, W.; Vasiliev, A. L.; Zhu, K.; Padture, N. P. Room-Temperature Crystallization of Hybrid-Perovskite Thin Films Via Solvent-Solvent Extraction for High-Performance Solar Cells. *J. Mater. Chem. A* **2015**, *3*, 8178−8184.

(23) Jeon, N. J.; Noh, J. H.; Kim, Y. C.; Yang, W. S.; Ryu, S.; Seok, S. I. Solvent Engineering for High-Performance Inorganic-Organic Hybrid Perovskite Solar Cells. *Nat. Mater.* **2014**, *13*, 897−903.

(24) Jung, J. W.; Williams, S. T.; Jen, A. K.-Y. Low-Temperature Processed High-Performance Flexible Perovskite Solar Cells via Rationally Optimized Solvent Washing Treatments. *RSC Adv.* **2014**, *4*, 62971.

(25) Zhou, Y.; Game, O. S.; Pang, S.; Padture, N. P. Microstructures of Organometal Trihalide Perovskites for Solar Cells: Their Evolution from Solutions and Characterization. *J. Phys. Chem. Lett.* **2015**, *6*, 4827−4839.

(26) Yang, M.; Zhou, Y.; Zeng, Y.; Jiang, C.-S.; Padture, N. P.; Zhu, K. Square-Centimeter Solution-Processed Planar $CH_3NH_3PbI_3$ Perovskite Solar Cells with Efficiency Exceeding 15%. *Adv. Mater.* **2015**, *27*, 6363−6370.

(27) Zhao, Y.; Nardes, A. M.; Zhu, K. Mesoporous Perovskite Solar Cells: Material Composition, Charge-Carrier Dynamics, and Device Characteristics. *Faraday Discuss.* **2014**, *176*, 301−312.

(28) Kulkarni, S. A.; Baikie, T.; Boix, P. P.; Yantara, N.; Mathews, N.; Mhaisalkar, S. Band-Gap Tuning of Lead Halide Perovskites Using a Sequential Deposition Process. *J. Mater. Chem. A* **2014**, *2*, 9221−9225.

(29) Weinberg, M. C.; Poisl, W. H.; Granasy, L. Crystal Growth and Classical Nucleation Theory. *C. R. Chim.* **2002**, *5*, 765−771.

(30) Shannon, R. D. Revised Effective Ionic Radii and Systematic Studies of Interatomic Distances in Halides and Chalcogenides. *Acta Crystallogr., Sect. A: Cryst. Phys., Diffr., Theor. Gen. Crystallogr.* **1976**, *32*, 751−767.

(31) Edward, J. T. Molecular Volumes and the Stokes-Einstein Equation. *J. Chem. Educ.* **1970**, *47*, 261−270.

(32) Zhou, Y.; Vasiliev, A. L.; Wu, W.; Yang, M.; Pang, S.; Zhu, K.; Padture, N. P. Crystal Morphologies of Organolead Trihalide in Mesoscopic/Planar Perovskite Solar Cells. *J. Phys. Chem. Lett.* **2015**, *6*, 2292−2297.

(33) De Yoreo, J. J.; Gilbert, P. U. P. A.; Sommerdijk, N. A. J. M.; Penn, R. L.; Whitelam, S.; Joester, D.; Zhang, H.; Rimer, J. D.; Navrotsky, A.; Banfield, J. F.; Wallace, A. F.; Michel, F. M.; Meldrum, F. C.; Cölfen, H.; Dove, P. M. Crystallization by Particle Attachment in Synthetic, Biogenic, and Geologic Environments. *Science* **2015**, *349*, aaa6760.

(34) Hu, M.; Bi, C.; Yuan, Y.; Bai, Y.; Huang, J. Stabilized Wide Bandgap $MAPbBr_xI_{3-x}$ Perovskite by Enhanced Grain Size and Improved Crystallinity. *Adv. Sci.* **2015**, DOI: 10.1002/advs.201500301.

(35) Hoke, E. T.; Slotcavage, D. J.; Dohner, E. R.; Bowring, A. R.; Karunadasa, H. I.; McGehee, M. D. Reversible Photo-Induced Trap Formation in Mixed-Halide Hybrid Perovskites for Photovoltaics. *Chem. Sci.* **2015**, *6*, 613−617.

(36) Suarez, B.; Gonzalez-Pedro, V.; Ripolles, T. S.; Sanchez, R. S.; Otero, L.; Mora-Sero, I. Recombination Study of Combined Halides (Cl, Br, I) Perovskite Solar Cells. *J. Phys. Chem. Lett.* **2014**, *5*, 1628−1635.

DOI: 10.1021/acsami.5b10987
ACS Appl. Mater. Interfaces 2016, 8, 2232−2237